From Electronic Structure to Design Principles for Photocathodes: Cu-Ba Alloys

I. A. Napier,[1,*] V. Chang,[2] T. C. Q. Noakes,[3] and N. M. Harrison[1]

[1] *Department of Chemistry, Imperial College London, White City Campus, 80 Wood Lane, London W12 0BZ, United Kingdom*

[2] *Department of Materials, Imperial College London, South Kensington, London SW7 2AZ, United Kingdom*

[3] *STFC Daresbury Laboratory and Cockcroft Institute, Daresbury, Warrington WA4 4AD, United Kingdom*

(Received 25 January 2019; revised manuscript received 2 April 2019; published 26 June 2019)

Producing a metal photocathode with a low work function (WF), low emissivity, and high quantum efficiency is a matter of importance in the design of the next generation of free-electron laser facilities. General rules for the design of appropriate materials are currently unclear and difficult to elucidate from observations of structure-composition relationships of known photocathodes. In this work, high-quality density-functional-theory electronic structure calculations and a simple physical model are employed to develop design rules for photocathodes based on metallic alloys. A theoretical study of metal alloys for photocathode applications is presented, in which high WF, stable copper is paired with low WF, unstable barium in two alloys, $Cu_{13}Ba$ and CuBa. Surfaces terminating in a plane of Ba atoms have a lower computed surface energy than those terminating in Cu atoms due to surface segregation of the larger Ba atoms. This results in a significant surface dipole due to the interatomic charge transfer from the differences in electronegativity of the species. The details of the surface structure determine the direction of the dipole and thus have a strong influence on the computed WF. The computed WF of the $Cu_{13}Ba$ Ba-terminated (100) surface is even lower than that of pure Ba, at 1.95 eV. The computed quantum efficiency (QE) of the best-performing pure Cu surface is 5.86×10^{-6}, whereas the best-performing $Cu_{13}Ba$ surface terminates in a plane of Ba atoms and has a significantly increased QE of 5.09×10^{-3}. A surface terminating in two planes of Ba atoms, the (001) surface of CuBa, has an even higher computed QE of 1.38×10^{-2}.

DOI: 10.1103/PhysRevApplied.11.064061

I. INTRODUCTION

Free-electron lasers (FELs) are single-pass machines that use unbound electrons to generate coherent, tuneable radiation from THz to x rays. Free electrons are generated by a photocathode, accelerated to relativistic speeds in a linear accelerator, and passed through an undulator where they form coherent bunches. The radiation emitted by these bunches of electrons has very high peak brightness, at least 9 orders of magnitude higher than state-of-the-art synchrotron sources [1], and is capable of femtosecond, or even attosecond time resolution [2]. An x-ray FEL can therefore explore chemical processes on their natural length and timescale, 1 Å and 1 fs, allowing information to be obtained in a manner that has not been possible to date.

In next-generation FELs, the quality of the electron beam determines the consistency, intensity, coherence, and time resolution properties of the radiation produced by the FEL. The photocathode, which is laser illuminated in an rf cavity, must exhibit a low work function (WF), a high quantum efficiency, be robust, have low emittance, and a fast response time. The development of such a photocathode is critical to the improvement of FEL facilities [3].

Currently, metal photocathodes are used due to their high durability and fast response time. For example, pure polycrystalline copper is currently used as the photocathode material in the FEL at the Linac Coherent Light Source at the SLAC National Accelerator Laboratory. Copper photocathodes have been shown to be stable for years in the vacuum of the rf-gun environment [4]. However, their quantum efficiency (QE), a measure of how many electrons are ejected from the photocathode per incident photon, is low compared to semiconducting photocathodes. The typical QE of a metal photocathode such as copper is on the order of 10^{-5}, whereas that of a typical semiconductor is much higher, on the order of 10^{-2} [3]. A high QE is desired to maximize the energy density in each bunch of the electron beam. Typically, metal photocathodes need to be driven by short wavelength UV lasers due to their high WF, the minimum energy required to extract an electron. But, the technical challenges of a suitable UV drive laser are vast so it is desirable for the cathode drive laser to operate at visible to near IR wavelengths [3]. This is

---

*i.napier17@imperial.ac.uk

© 2019 American Physical Society

facilitated by a cathode with low WF and high QE that emits an electron beam of exceptional quality.

Numerous techniques have been trialed to reduce the WF and increase the QE of metal photocathodes. Recent examples include coating them with atomically thin two-dimensional (2D) nanomaterials [4], and using computational design to simulate oxide thin films such as MgO and BaO on Ag(100) [5].

It has been shown that the QE of the metal-based alloys Mg-Ba and Al-Li is significantly higher than Mg and Al [6]. It has also been shown that alloying low-melting point metals (Pb, Bi, Ga, In) with alkali metals, results in a drastic decrease in the WF at low concentrations of the alkali metal. This has been explained, in part, by the significant change in the lattice parameters induced by alkali metal doping [7].

A. General considerations

An alternative approach is to use a metal with a low WF such as Ba, with a WF of about 2.5 eV, compared to about 4.7 eV for Cu. Ba is, however, extremely reactive and easily oxidized, and the oxidized surface is both unpredictable in application and has a significantly increased WF, making the pure metal unsuitable for photocathode applications.

However, chemical stability may be able to be achieved by alloying with a very stable metal. Charge transfer may also be possible between the metals, which could be used to reduce the surface potential and result in a low WF alloy. Surface segregation could also be used to change the surface composition, while maintaining the long-range order of the bulk alloy. These desirable properties suggest alloying two metals with very different electronegativities and atomic radii.

In the current work, a photocathode design strategy based on alloying a high WF, stable metal (Cu) with a low WF, chemically unstable metal (Ba) is explored. Two stable alloys, $Cu_{13}Ba$ and CuBa, are known according to the phase diagram by Braun and Meijering [8]. A detailed theoretical study of these alloys and their surface terminations establishes the relationship between alloy composition, surface structure, and the resultant WF and QE. In addition to suggesting a promising photocathode material, this work suggests an alternative approach to photocathode design.

II. COMPUTATIONAL DETAILS

Density-functional-theory (DFT) calculations are carried out using CASTEP 8.0 [9]. A plane-wave basis set is used with ultra-soft pseudopotentials generated on the fly by CASTEP to approximate the properties of the core electrons. Electronic exchange and correlation are computed in the generalized gradient approximation (GGA) using the PBEsol functional [10]. This functional is chosen because it is designed for solid-state and surface systems and is found to reproduce the experimental lattice constants and surface energies well.

The number of k-points required to sample the Brillouin zone is implemented using the Monkhorst-Pack (MP) [11] method and a smearing width of 300 K is introduced to converge the total energy. Electronic optimization is terminated when three consecutive total energy calculations are within 10^{-8} eV per atom. The convergence criteria for geometry optimization calculations are 0.001 Å for displacement distance and 0.05 eV/Å for forces between atoms.

Thickness of the slabs is increased until the separation of the central layers reproduced those of the bulk material.

The surface energy, γ, is given by

$$\gamma = \frac{E_{\text{slab}} - nE_{\text{bulk}}}{2A}. \qquad (1)$$

E_{slab} is the energy of a slab of n layers, E_{bulk} is the energy associated with the bulk material, and A denotes the 2D surface area of the surface unit cell.

Using a 550 eV cutoff energy for bulk Cu, Ba, $Cu_{13}Ba$, and CuBa, the total energy is converged to 1 meV/atom. The k-point grid is varied for each material based on the unit-cell dimensions until convergence of 0.1 meV/atom is achieved.

Surfaces are simulated as 2D periodic slabs, which, for computational convenience, are represented as a three-dimensional (3D) periodic series of stacked slabs of solid material separated by vacuum gaps (the so-called 3D periodic slab model). The key parameters governing the extent to which this model represents the free surface of the bulk crystal are the thickness of the slab and the size of the vacuum gap. The thickness of the slabs is found by converging their surface energies to within 10^{-3} J/m^2. Terminations are chosen to ensure the slabs are symmetrical, as necessitated by the 3D periodic slab model, since the two surfaces of the slab exposed to the vacuum must be identical. The size of the vacuum gap is increased until the charge density is close to zero in the middle of the gap, ensuring no interaction between adjacent surfaces.

The Cu slabs are 14 atomic layers thick with a vacuum region of 20 Å between repeating slabs, and the Ba surfaces are composed of 12 layers and a 25 Å vacuum. The displacement upon relaxation of atoms in the center of the slab vs the bulk interplanar distance is found to be less than 1%.

The $Cu_{13}Ba$ slabs, those cut by the (100), (110), and (111) Miller planes, are 13 layers thick with a vacuum region of 20 Å and the CuBa slabs, those cut by the (001), (100), and (101) Miller planes, used a vacuum region of 25 Å.

Three different terminations exist for the CuBa slabs cut by the (001) plane; two Ba-terminated surfaces and one Cu-terminated surface. Of the two Ba-terminated slabs, the

TABLE I. Experimental [18,19] and computed lattice parameters for the conventional copper and barium unit cells, measured in Å.

	PBEsol (this work)	Expt	$\Delta_{\mathrm{PBEsol-Expt}}$
Copper	3.561	3.597	1.00%
Barium	5.028	5.015	0.26%

first has one layer of Ba atoms on the surface (one Ba), and the other has two layers of Ba atoms (two Ba). The one-Ba termination is 15 layers thick, the two-Ba surface is 17 layers thick, the Cu-terminated surface is 13 layers thick, and the (100) and (101) surfaces are 23 and 32 layers thick, respectively.

The WF is estimated from the DFT eigenvalues as the difference between the Fermi energy and the average potential in the center of the vacuum region of the 3D periodic cell.

The photoemission model used to study QE of the metal and alloy surfaces is developed by Camino [12], based on Spicer's three-step model [13]. Camino's model allows the QE to be decomposed into contributions from each atomic layer and assumes electrons are excited to the conduction band and, if the final state is above the vacuum level, an electron can be emitted. This is supported by the experimental evidence [14,15]. The inelastic mean free path (IMFP) of the photoexcited electrons is calculated using the theoretical method described by Nagy and Echenique [16]. The IMFP of Cu and Ba is estimated to be 3.00 and 2.14 Å, respectively.

A photon energy of 4.7 eV is specified for QE measurements since this is approximately the energy emitted from the third harmonic of a Ti:sapphire laser, as used in the CLARA FEL at Daresbury Laboratory [17].

III. RESULTS AND DISCUSSION

A. Pure copper and barium

Copper adopts the fcc structure, belonging to space group 225. Barium adopts the bcc structure and belongs to space group 229. Their lattice parameters have been determined by x-ray diffraction at room temperature in Refs. [18] (Cu) and [19] (Ba). These parameters are compared to the calculated lattice parameters and are reproduced to within 1% by the computed values (Table I).

The experimental lattice parameters are reproduced with typical accuracy for DFT by the calculations employed in this work, varying by 1% or less. Surface relaxation is also studied and is consistent with previous findings for Cu, although no previous work on Ba low-index surface relaxation could be found. These results are summarized in Table II. The variation in the interlayer spacing between the bulk and the center of each simulated slab is below 1%, indicating the slab is of sufficient thickness to effectively simulate the bulk material at its center. As discussed by Rodach *et al.*, the general trend is reproduced quite well compared to the EAM, however the absolute values differ and even values reported by Foiles *et al.* differ substantially from those obtained by Ning *et al.* using the same method. Compared to the more modern calculations using the PAW method by Punkkinen *et al.*, the general trends are well reproduced, with a smaller discrepancy in absolute values. For both Cu and Ba, the relaxation decays quickly with increasing distance from the surface, becoming more and more like the bulk interlayer spacing towards

TABLE II. Calculated layer relaxations for the low-index surface of Cu and Ba, given as a percentage of the bulk interlayer spacing. δ_{c-b} indicates the difference in interlayer spacing between the center of the slab and the relevant bulk parameter, as calculated in this work.

	Cu(100)				Cu(110)				Cu(111)			
	δ_{c-b}	δ_{12}	δ_{23}	δ_{34}	δ_{c-b}	δ_{12}	δ_{23}	δ_{34}	δ_{c-b}	δ_{12}	δ_{23}	δ_{34}
This work	0.05	−2.29	1.10	0.15	−0.70	−9.62	4.42	−1.24	−0.01	−0.84	0.24	0.08
LDA[a] [20]	-	−3.02	0.08	−0.24	-	−9.27	2.77	−1.08	-	−1.27	−0.64	−0.26
PAW[b] [21]	-	−1.20	0.03	0.58	-	-	-	-	-	−0.31	0.04	0.31
EAM[c] [22]	-	−3.79	−0.54	0.02	-	−8.73	1.56	1.20	-	−2.48	−0.04	0.00
Expt.	-	−1.10[d]	1.70[d]	-	-	−8.50[e]	2.30[e]	-	-	−0.70[f]	-	-
	Ba(100)				Ba(110)				Ba(111)			
	δ_{c-b}	δ_{12}	δ_{23}	δ_{34}	δ_{c-b}	δ_{12}	δ_{23}	δ_{34}	δ_{c-b}	δ_{12}	δ_{23}	δ_{34}
This work	0.55	4.46	−4.39	1.97	0.00	0.06	0.10	−0.03	−0.42	23.27	−31.73	5.74

[a] Local-density approximation.
[b] Projector-augmented-wave method.
[c] Embedded-atom method.
[d] Experiment, Ref. [23].
[e] Experiment, Ref. [24].
[f] Experiment, Ref. [25].

TABLE III. Comparison of surface energies and work function for the low-energy surfaces of Cu and Ba.

	Copper			Barium		
	(100)	(110)	(111)	(100)	(110)	(111)
Surface energy (J/m^2)	1.83	1.93	1.66	0.37	0.55	0.45
Previous calculations	1.76[a]	1.88[a]	1.59[a]	0.42[b]	0.41[b]	0.50[b]
	2.15[b]	2.19[b]	1.94[b]	0.35[c]	0.38[c]	0.40[c]
Experiment	-	-	1.83[d]	-	0.38[e]	-
$\Delta_{\text{this work}-\text{prev. calc.}^{\text{a(Cu) and b(Ba)}}}$ (%)	3.8	2.6	4.2	11.9	14.0	10.0
WF (eV)	4.46	4.40	4.73	2.22	2.32	2.30
Previous calculations	4.43[a]	4.48[a]	4.98[a]	2.31[b]	2.38[b]	2.29[b]
Experiment	4.59[f]	4.48[f]	4.94[f]	-	-	2.70[g]
$\Delta_{\text{this work}-\text{prev. calc.}}$ (%)	0.7	1.8	5.0	3.9	2.5	0.4

[a] PBEsol functional, Ref. [29].
[b] PBE functional, Ref. [30].
[c] Full charge density method, Ref. [31].
[d] Experiment, Ref. [32].
[e] Experiment, Ref. [33].
[f] Experiment, Ref. [34].
[g] Experiment, Ref. [35].

the center of the simulated material. The Ba(111) face demonstrates large surface relaxations due to its low packing density. Other bcc metals, such as Nb, W, and Fe, also show large surface relaxations where the spacing of the top two or three layers varies drastically compared to the bulk interlayer spacing [26–28].

The surface energy and WF of the bulk terminated but fully relaxed slabs cut along the (100), (110), and (111) Miller planes are reported in Table III. They are compared to previous calculations and experimental values deduced from liquid surface-tension measurements.

For the Cu surfaces, the computed surface energies are in good agreement with the results from a similar theoretical study, the values all within 5% of each other [29]. For the Ba surfaces the agreement is less good, surface energies differing by 10%–14% from values found by Wang and Wang [30] and Vitos *et al.* [31].

All calculated WF values are within 5% of previous theoretical works [29,30]. When comparing WF values to those obtained from experiment, one must keep in mind surface reconstruction and/or contamination can significantly affect the observed values. For example, the WF of metals that absorb gases such as O_2 strongly is very sensitive to the measurement and preparation environments. For example, Delchar found that the WF of the Cu (100) surface increased from 4.6 to 4.9 eV in the presence of a $(\sqrt{2}\times\sqrt{2})$R45° oxygen overlayer [36]. Thus care must be taken when comparing the computed WF for an idealized model of a surface and that measured on a particular sample.

The QE of the low-energy Cu and Ba surfaces are summarized in Table IV. The Ba surfaces have a much higher QE than the Cu surfaces, the main contributing factor being the difference in WF.

B. Bulk alloy structures

The Cu-Ba phase diagram contains two stable alloys, $Cu_{13}Ba$ and CuBa [37]. $Cu_{13}Ba$ is 93 at.% copper, but the 7 at.% barium has a profound influence on the properties of the material. For example, the melting point is reduced compared to pure copper, from 1085 °C to the peritectic transformation temperature of 758 °C. As Jesche *et al.* [37] have demonstrated, single crystals of $Cu_{13}Ba$ can be easily grown in the laboratory due to the deep eutectic in the phase diagram.

Crystals of $Cu_{13}Ba$ belong to space group 226, characterized by the fcc $NaZn_{13}$ structure type. The calculated optimized lattice parameter is 11.532 Å, which is in good agreement with that determined by x-ray diffraction at room temperature of 11.697 Å (1.4% higher, Wendorff and Röhr [38]) and 11.719 Å (1.6% higher, Braun and Meijering [8]). The unit cell is visualized in Fig. 1.

The crystal structure of the 50/50 mixture, CuBa, belongs to space group 194 and consists of close-packed planes of trigonal prisms of Ba, with Cu at their center, arranged along the (001) direction. Chakrabarti and Laughlin [39] found that weak Ba—Ba bonds exist between planes, meaning the alloy behaves as a layered structure. Figure 2 displays the conventional unit cell, as well as two

TABLE IV. Calculated QE values for the low-energy surfaces of pure Cu and Ba.

	Cu			Ba		
	(100)	(110)	(111)	(100)	(110)	(111)
QE ($\times 10^{-7}$)	0.84	7.67	58.60	-	-	-
QE ($\times 10^{-3}$)	-	-	-	8.75	6.49	7.78

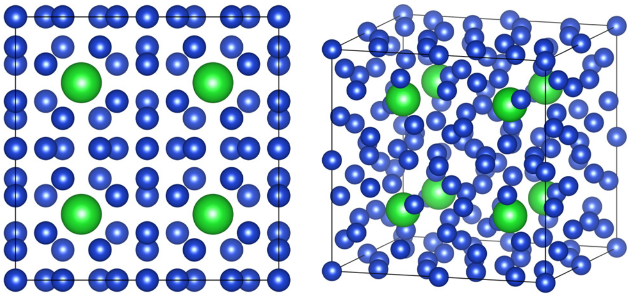

FIG. 1. The unit cell of $Cu_{13}Ba$, looking along a crystallographic (100) axis (left) and in perspective (right). There are 112 atoms in the conventional unit cell; 104 Cu atoms (blue) and 8 Ba atoms (green).

representations where the unit cell is expanded by a factor of 3 in all directions to highlight the layered structure and hexagonal symmetry.

The unit cell is characterized by the lattice parameters $a = b \neq c$, and $\alpha = \beta = 90^\circ$, $\gamma = 120^\circ$. The lattice parameters a and b are calculated to be 4.376 Å and c is found to be 16.211 Å. The experimental values deduced from x-ray diffraction [40] are $a = b = 4.499$ Å and $c = 16.250$ Å, differing by 2.7% and 0.2%, respectively, from the calculated parameters.

C. $Cu_{13}Ba$ surfaces

The low-energy surfaces are those cut by the (100), (110), and (111) Miller planes from the bulk crystal. The formation energy, $E_{\text{formation}}$, is calculated with regard to the energy per atom of bulk Cu ($E_{\text{Cu atom}}$) and Ba ($E_{\text{Ba atom}}$):

$$E_{\text{formation}} = \frac{E_{\text{slab}} - (n\text{Cu} \times E_{\text{Cu atom}}) - (n\text{Ba} \times E_{\text{Ba atom}})}{2A}, \tag{2}$$

where E_{slab} is the energy of the $Cu_{13}Ba$ slab and nCu and nBa is the number of Cu or Ba atoms in that slab. $E_{\text{Cu atom}}$ and $E_{\text{Ba atom}}$ denote the energy associated with one Cu or Ba atom in bulk Cu or Ba. This definition allows the formation energy of surfaces with different stoichiometries to be compared.

TABLE V. Comparison of formation energies and work function for the low energy surfaces of $Cu_{13}Ba$.

	(100)		(110)	(111)
Terminating atom	Ba	Cu	Cu	Cu
$E_{\text{formation}}$ (J/m^2)	0.69	1.75	1.90	1.55
WF (eV)	1.95	4.31	4.29	3.92
QE ($\times 10^{-4}$)	50.9	1.52	0.84	2.47

For the (100) slab, there are two bulk terminations that resulted in symmetric surfaces. One termination places barium atoms on the surface, and the other termination places copper atoms on the surface. Table V contains results of calculations of formation energy and WF for each slab.

The computed WF of the (110) and (111) slabs is between that of the WF of the corresponding pure Cu and Ba slabs. This is consistent with a generalization of Vegard's law to the WF since the unit cell of $Cu_{13}Ba$ surfaces is mostly composed of Cu, so the properties may be expected to closely align with those of pure Cu. The result for the (100) slab, with its Ba and Cu terminations is, however, not consistent with this simple model, as seen in Fig. 3.

The WF of the Cu-terminated (100) slab is, again, similar to that of the Cu-terminated (110) and (111) slabs. However, the WF of the Ba-terminated (100) slab is much lower, 1.95 eV, which is even lower than that of the pure Ba (100) slab (2.22 eV). This unexpected result can be rationalized by looking at the charge distribution within the alloy.

The Pauling electronegativity of Ba is 0.89, whereas Cu has a value of 1.90. One therefore expects a significant charge transfer from Ba to Cu in the alloy. A Bader charge analysis [41] revealed that, in the bulk, each Cu atom has 0.09 more electrons in its Bader volume and each Ba atom had 1.19 fewer. The results are shown in Table VI. The

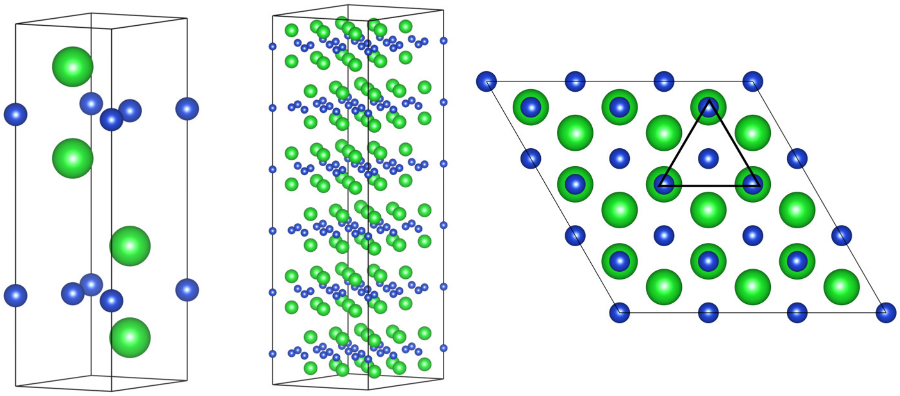

FIG. 2. The conventional unit cell of CuBa (left). There are four of each species in the unit cell, which is expanded by a factor of 3 in all directions (middle and right). The black triangle highlights the hexagonal symmetry.

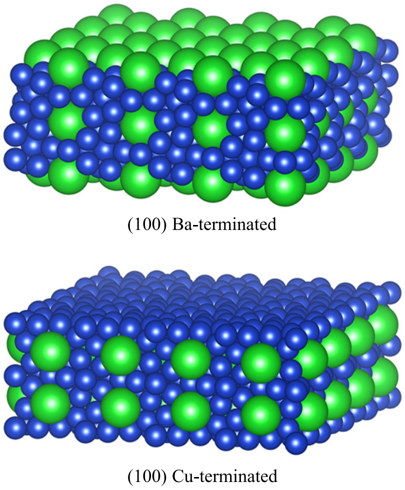

FIG. 3. The $Cu_{13}Ba$ Ba-terminated surface (top) and the Cu-terminated surface (bottom). The unit cell is repeated four times in the *a* and *b* directions to highlight the different terminations.

Ba-terminated (100) slab exhibits the lowest formation energy, 0.69 J/m^2. This suggests that even in somewhat disordered and granular materials the Ba atoms are likely to segregate to free surfaces and grain boundaries. This is also consistent with the general tendency of larger atoms in alloys to surface segregate [42].

The Bader analysis suggests that the bulk crystal can be considered to be $Ba^{+1.19}$ and $Cu^{-0.09}$. The average charge on each atom is similar for the surfaces and bulk. This nonuniform charge distribution can generate a significant surface dipole depending on the details of the surface termination and structure. If the dipole is thought of as going from an area of net negative charge to an area of net positive charge, then it is pointing into the surface for each slab; except for the (100) Ba-terminated slab, where the dipole is pointing out of the surface. This results in a large reduction in the WF of the Ba-terminated (100) surface, in contrast to each of the Cu-terminated slabs for which the WF is increased.

It has previously been observed that organic dipole layers on Au and Ag reduced their WF, and a linear relationship existed between the size of the surface dipole moment and WF [43]. It has also been reported that the WF of an indium-tin oxide electrode could be reduced if the dipole vector due to a self-assembled monolayer (SAM) is pointing away from the electrode-SAM interface [44]. In the context of the current results, this suggests a general design principle for decreasing the WF of alloy surfaces by engineering structures with large interatomic charge transfer and surface dipoles.

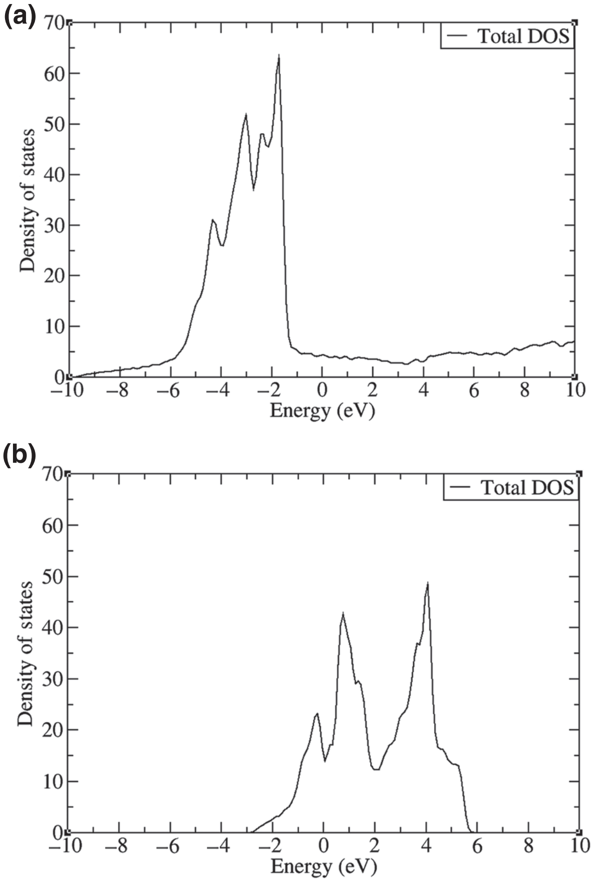

FIG. 4. Density of states (DOS) of (a) Cu(100) and (b) Ba(100) slabs. Cu has a large DOS below the Fermi energy and Ba exhibits a large DOS below the photon energy.

In addition to a reduction in WF by specific surfaces, the DOS should be considered. The process occurring in step one of Spicer's three-step photoemission model is excitation of electrons from the valence band to conduction band. In order for the QE to be maximized, the DOS should be large in energy regions where electrons are being excited from and there should also be a large number of states electrons can be excited into.

Electrons can be excited to any state between the Fermi energy and the photon energy (properly weighted by

TABLE VI. Bader charge analysis of the $Cu_{13}Ba$ slabs and bulk. The values correspond to the average number of extra electrons associated with each element.

	(100)		(110)	(111)	Bulk
Terminating atom	Ba	Cu	Cu	Cu	-
Extra electrons per Cu atom	+0.14	+0.08	+0.06	+0.09	+0.09
Extra electrons per Ba atom	−1.20	−1.19	−1.18	−1.25	−1.19

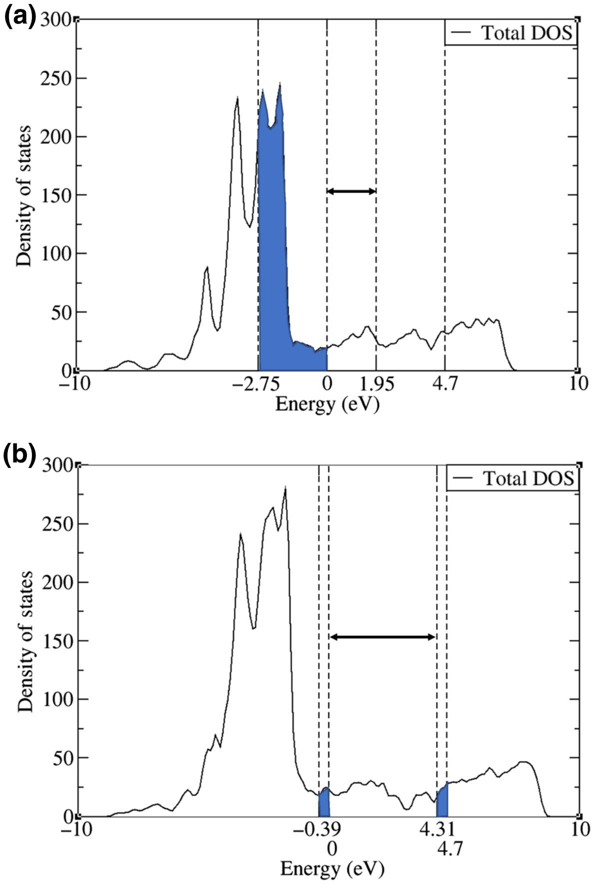

FIG. 5. DOS of the $Cu_{13}Ba$ (100) Ba-terminated (a) and Cu-terminated (b) slabs. The highlighted regions correspond to the states electrons can be excited from and into. The states able to participate in electron excitation are much larger when the WF is lower.

the Fermi golden rule). However, only electrons that are excited to states above the WF can be emitted: a small fraction of the total excited electrons.

In order to maximize the QE, the number of allowed transitions, the number of states from which a photoexcited electron can be emitted, and the number of photoexcited electrons need to be maximized.

It is possible, therefore, to use the DOS of the pure metal as a guide to the QE of the alloy. Figure 4 shows the computed DOS of the (100) slabs of pure Cu and Ba, revealing a large DOS on Cu in the energy interval below the Fermi energy and a large DOS in the region below the photon energy on Ba. Mixing these two in an alloy, $Cu_{13}Ba$, yields the DOS plotted in Fig. 5, with a large number of states in the required regions, highlighted in blue.

It is clear that combining Cu and Ba gives rise to a greater DOS in the required regions compared to pure Cu and Ba alone. Significantly more electrons are therefore available to be excited and emitted from the alloy compared to the pure metals.

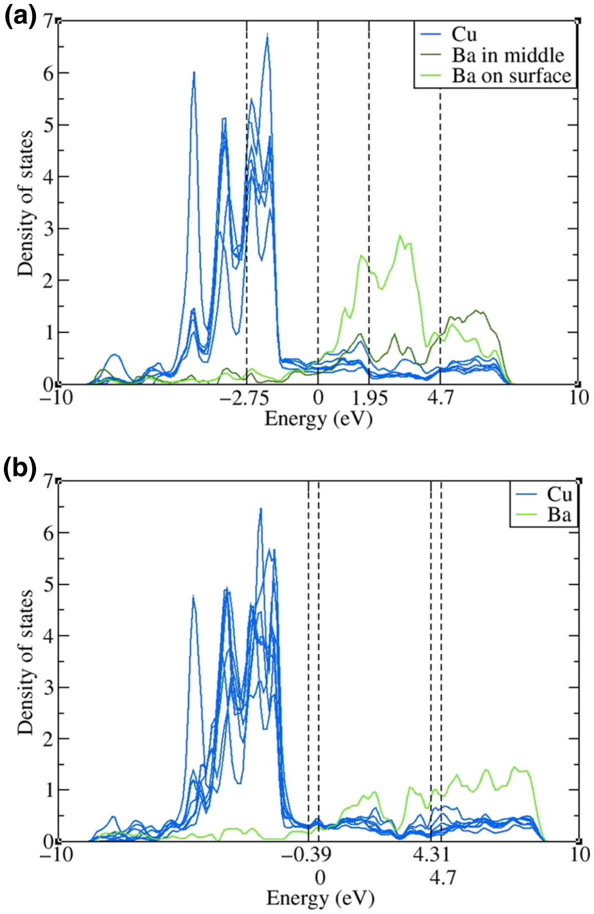

FIG. 6. DOS of the $Cu_{13}Ba$ Ba-terminated (a) and Cu-terminated (b) (100) slabs projected onto the different types of atoms. (a) The blue lines relate to the electronic states localized on different Cu atoms, the light green trace denotes the states localized on Ba atoms at the surface, and the dark green trace is the states localized on Ba atoms buried in the center of the slab. (b) The blue trace is the Cu atoms and the green trace is the Ba atoms towards the center of the slab. Only one type of Ba atom exists in this slab.

The QE of each slab is summarized in Table V. The Ba-terminated (100) slab exhibits the highest QE, expected due to its low WF and large DOS in the relevant regions. This slab has a QE over 30 times higher than the Cu-terminated (100) slab, and the (110) and (111) slabs perform similarly poorly by comparison. The main explanation for the poor QE observed for the Cu-terminated slabs is their high WF compared to the Ba-terminated (100) slab. The WF of these slabs is so much higher due to the fact that their dipole vector points into the surface, hindering photoemission. The high WF also means a smaller number of states are available to participate in the photoemission process, as seen in the highlighted regions of Fig. 5, where the DOS of the low WF Ba-terminated (100) slab and the high WF Cu-terminated (100) slab are compared.

TABLE VII. Formation energies, WF, QE, and interplanar distance of the low-energy CuBa surfaces.

	(001)			(100)	(101)
Termination	One Ba	Two Ba	Cu	Cu/Ba	Cu/Ba
$E_{\text{formation}}$ (J/m^2)	0.23	0.43	1.55	0.48	0.61
WF (eV)	2.36	2.20	4.21	2.43	2.86
QE ($\times 10^{-3}$)	6.53	13.80	0.08	1.51	0.5

Compared to pure Cu, the WF of the best-performing surface studied here, $Cu_{13}Ba$, is over 850 times higher than the best-performing Cu surface. Even the worst-performing $Cu_{13}Ba$ surface, (110), has a QE over 14 times higher than the best pure Cu surface. It is therefore clear that alloying Cu with a small amount of Ba has the potential to drastically improve its QE.

More information can be gleaned from the projected DOS (PDOS), the DOS projected onto the different types of atoms in each slab. Figure 6 compares the PDOS of the Ba-terminated and the Cu-terminated (100) slabs. The dashed lines denote the states electrons can be emitted from and into during an excitation. Aside from the much larger number of states available to participate in an excitation, the Ba-terminated slab has a large number of states localized on the surface of the slab. These can be seen in image (a) of Fig. 6, in the region from 1.95–4.70 eV, which is highlighted in light green. If an electron is excited from states below the Fermi energy, localized on Cu atoms, they are most likely to be excited into states localized on Ba atoms on the surface of the slab due to their large contribution to the PDOS. Electrons excited to these states at the surface of the crystal are likely to be emitted with insignificant inelastic scattering and thus contribute to the QE. This can be compared to the Cu-terminated slab, where the states able to accommodate excited electrons are located in the center of the slab, meaning electrons will have a longer path to the vacuum and are less likely to escape, resulting in a smaller QE for this slab.

D. CuBa surfaces

The low-energy surfaces of CuBa are those cut by the (001), (100), and (101) Miller planes from the bulk crystal. Three different terminations exist for the (001) slab, two Ba-terminated surfaces and a Cu-terminated surface. Of the two Ba-terminated slabs, one has a single layer of

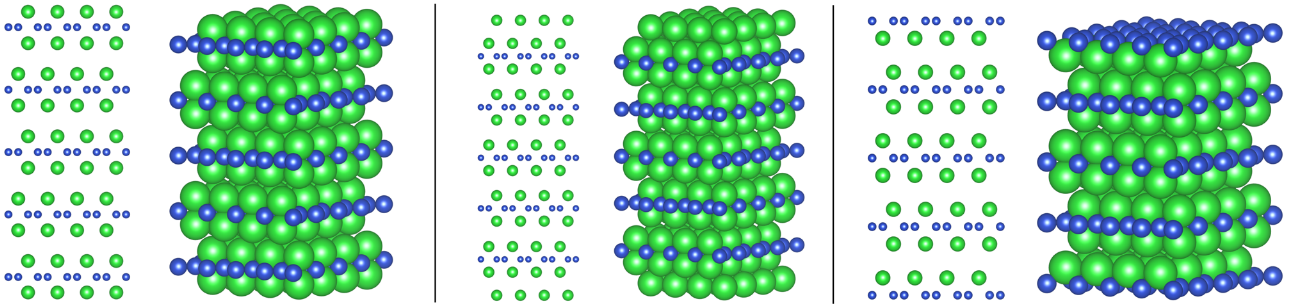

(001) One-Ba-terminated (001) Two-Ba-terminated (001) Cu-terminated

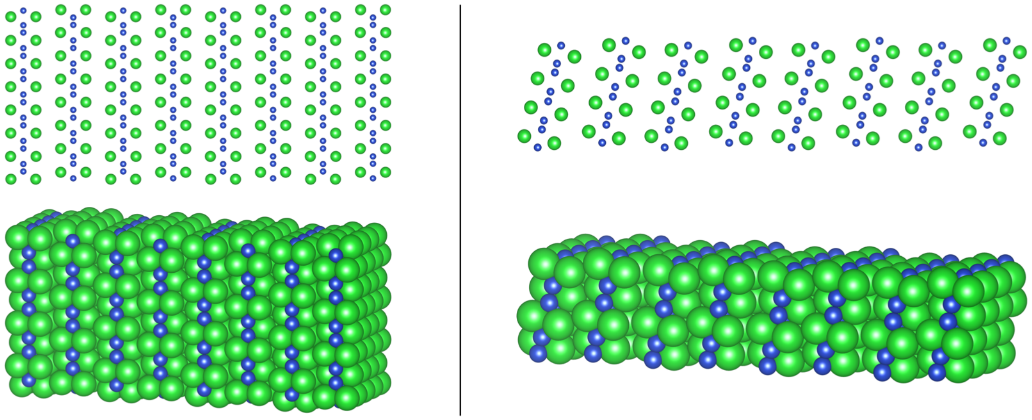

(100) (101)

FIG. 7. Low-energy CuBa surfaces. The three possible symmetrical terminations of the surface cut by the (001) plane are shown, along with the (100) and (101) slabs. Each unit cell is shown from the side and in perspective, as well as repeated four times in the x and y directions to give a feel for the nature of the surface of each slab.

TABLE VIII. Bader charge analysis of CuBa surfaces. The values correspond to the average number of electrons associated with each element.

	(001)			(100)	(101)	Bulk
Termination	One Ba	Two Ba	Cu	Cu/Ba	Cu/Ba	-
Extra electrons per Cu atom	+0.68	+0.67	+0.56	+0.73	+0.72	+0.67
Extra electrons per Ba atom	−0.68	−0.56	−0.70	−0.68	−0.72	−0.23

Ba atoms on the surface (one Ba), and the other has two layers of Ba atoms (two Ba).

The formation energy and WF of each slab is found in Table VII and the slabs are visualized in Fig. 7.

Formation energies are calculated in the same manner as for the $Cu_{13}Ba$ slabs. Similar to the $Cu_{13}Ba$ slabs, the slabs with Ba atoms on the surface have the lowest energy, suggesting Ba is likely to surface segregate in crystallites of the alloy.

The WF of the slabs is also in agreement with findings from the $Cu_{13}Ba$ slabs. The Ba-terminated slabs show a much smaller WF than the Cu-terminated slabs, due to the direction of the surface dipole. Results from a Bader charge analysis are summarized in Table VIII and confirms the existence of a surface dipole for each slab. In the bulk, each Ba atom in CuBa has 0.23 electrons fewer than normal, which can be compared to each Ba atom in $Cu_{13}Ba$ where 1.19 fewer electrons than usual are present. The charge distribution is less polarized for CuBa than $Cu_{13}Ba$ and net charges are not equal in the case of some slabs since the 1:1 stoichiometry is not maintained.

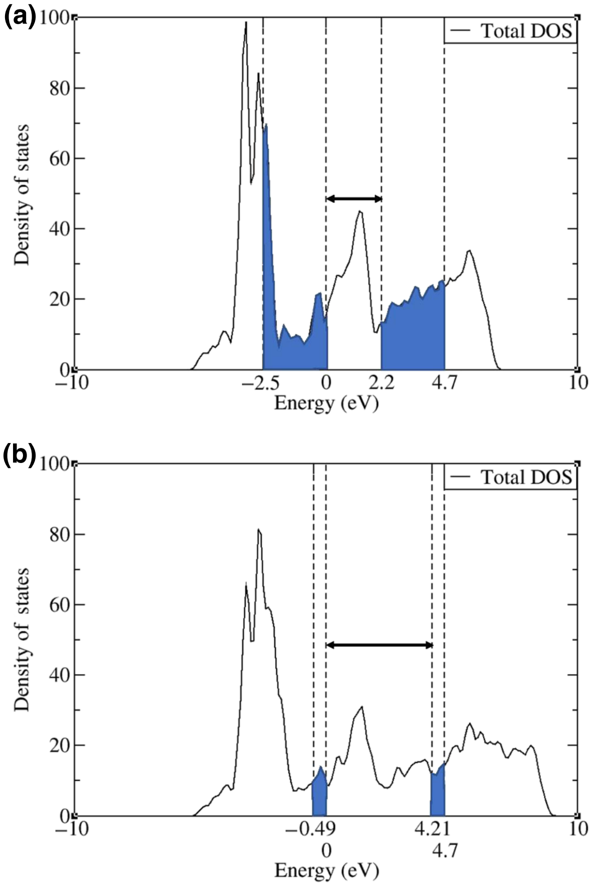

FIG. 8. DOS of two different CuBa surfaces. (a) Two-Ba-terminated (001) surface with regions electrons may be excited from and into are highlighted in blue. (b) The Cu-terminated (001) surface, showing that a higher WF leads to a smaller number of states available to participate in the excitation process.

The DOS of the two-Ba (001) and Cu-terminated (001) slabs are compared in Fig. 8. As for the $Cu_{13}Ba$ slabs, the low WF of the two-Ba (001) slab also means that more states are available to participate in photoemission than the high WF Cu-terminated (001) slab. The QE values (Table VII) reflect this observation, showing the slab terminating with two layers of Ba atoms has a high QE of 1.38×10^{-2}.

Again, in a similar fashion to the $Cu_{13}Ba$ slabs, the PDOS of the two-Ba (001) slab in Fig. 9 reveals that of the empty states into which electrons can be excited many are localized on surface Ba atoms.

These Ba atoms are on or near the surface, meaning excited electrons at the surface of the crystal are likely to be emitted with insignificant inelastic scattering and thus contribute to the QE. The available states for electrons to photoexcite into on the Cu-terminated (001) slab are localized mainly on Ba atoms, which are not on the surface of the slab, resulting in a longer path to the vacuum for excited electrons and thus a lower QE.

E. Oxygen adsorption

In the alloy, Ba is acting as a reductant, meaning the Ba-terminated surfaces may be less likely to suffer from oxidation than pure Ba since the Ba atoms on the surface of the alloy slab are already electron deficient. The computed charge of the surface Ba for the $Cu_{13}Ba(100)$ Ba-terminated surface and CuBa(001) one-Ba-terminated surface (which have the lowest formation energy) is 1.20 and 0.68 less electrons respectively, compared to pure Ba.

Calculations of oxygen adsorption onto both $Cu_{13}Ba$ (100) and CuBa(001) Ba-terminated surfaces show that adsorption to hollow sites is more energetically favorable than adsorption to top sites. These sites are visualized in Fig. 10.

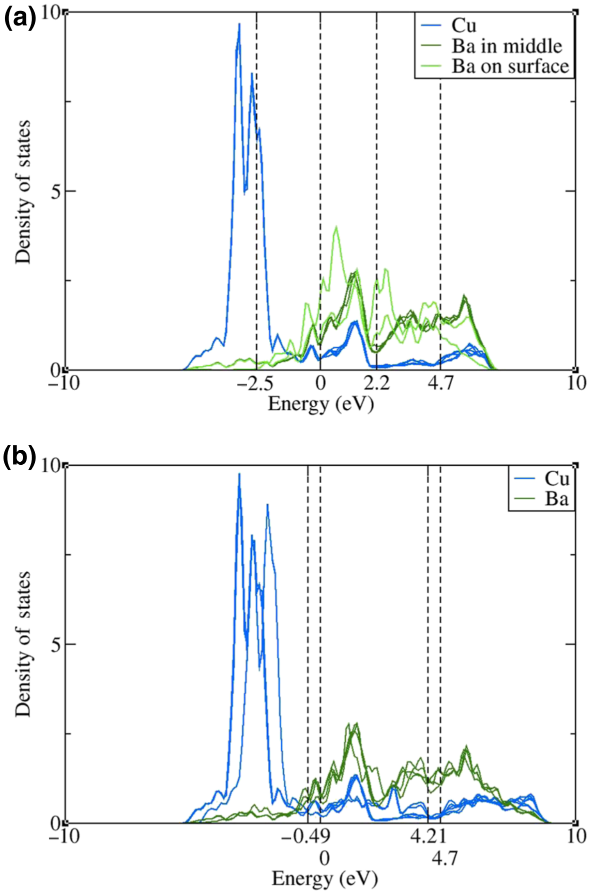

FIG. 9. PDOS of two different CuBa surfaces. (a) Two-Ba-terminated (001) surface with the DOS projected onto the different types of atoms. The two layers of Ba atoms are shown in light green, and the contribution to the DOS from the Ba atoms in the middle of the slab are shown by the dark green lines. (b) The Cu-terminated (001) surface. The Ba atoms are not on the surface so are all shown in dark green.

Average binding energies per oxygen adatom, E_b^O, are given relative to the clean surface and an isolated oxygen molecule:

$$E_b^O = -\frac{1}{N_O}\left(E_{O/\mathrm{surface}} - E_{\mathrm{surface}} - \frac{N_O}{2}E_{\mathrm{O}_2}\right), \qquad (3)$$

where N_O is the number of adsorbed oxygen atoms, $E_{O/\mathrm{surface}}$ is the total energy of the adsorbate-surface system, E_{surface} is the total energy of the clean surface, and E_{O_2} is the computed energy of an isolated oxygen molecule using the same computational details as for the bulk and surface calculations. It is well known that the GGA functional gives an overestimation of the O_2 binding energy [45]. Nevertheless, this does not affect the main purpose of this work.

The computed binding energy suggests that oxygen is most strongly bound in hollow sites. For $\mathrm{Cu}_{13}\mathrm{Ba}$ (Table IX), adsorption to hollow sites increased the WF from 1.95 eV for the clean surface, to 2.45 eV for a 1-monolayer (ML) covering. Lower coverages of 0.5 ML and 0.25 ML yielded smaller binding energies per adatom and lower WF values compared to the 1-ML covering. The QE of this surface is slightly reduced, from 5.09×10^{-3} for the clean surface to 4.45×10^{-3} for the 1-ML covering. This slight reduction in QE is thought to result from the reduction in the strength of the surface dipole that yields to an increase in the WF.

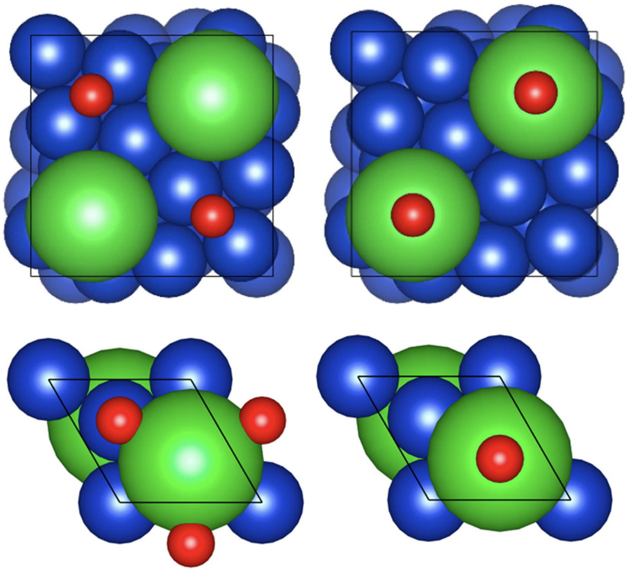

FIG. 10. Hollow sites (top left) and top sites (top right) on the surface of $\mathrm{Cu}_{13}\mathrm{Ba}(100)$ and hollow sites (bottom left) and top sites (bottom right) CuBa(001) Ba-terminated.

For CuBa (Table X), adsorption to hollow sites reduces the WF from 2.36 eV for the clean surface, to 1.38 eV for a 1-ML covering. Lower coverages of 0.5 ML and 0.25 ML yielded higher binding energies per adatom and increased WF values compared to the 1-ML covering. The lower WF for a 1-ML covering is due to the formation of a nonpolar BaO monolayer. Experimental and theoretical studies of metal oxide thin films on metal surfaces has shown that the metal oxide thin film tends to reduce the WF of the metal substrate [5,46,47]. This effect

TABLE IX. WF, QE, and binding energy of oxygen atoms E_b^O on the $\mathrm{Cu}_{13}\mathrm{Ba}(100)$ Ba-terminated surface for different coverage.

O/$\mathrm{Cu}_{13}\mathrm{Ba}$ (100)	ML	WF (eV)	E_b^O (eV)	QE ($\times 10^{-3}$)
Hollow	1.00	2.45	3.87	4.45
	0.50	2.25	1.89	4.70
	0.25	2.09	1.88	3.03
Top	1.00	7.24	−1.85	0
	0.50	5.02	−0.32	0
	0.25	3.54	−0.13	-
Hollow+top	1.00	7.52	1.33	0

TABLE X. WF, QE, and binding energy of oxygen atoms E_b^O on the CuBa(001) Ba-terminated surface for different coverages.

O/CuBa (001)	ML	WF (eV)	E_b^O (eV)	QE
Hollow	1.00	1.38	3.87	4.43×10^{-3}
	0.50	2.05	3.95	2.65×10^{-3}
	0.25	2.23	3.99	4.70×10^{-4}
Top	1.00	8.80	−1.63	0
	0.50	5.85	0.47	0
	0.25	3.60	1.04	-

has been experimentally demonstrated in previous measurements of WF from BaO thin films [48]. The QE of this surface is slightly reduced, from 6.53×10^{-3} for the clean surface to 4.43×10^{-3} when covered in 1 ML and it is reduced significantly to 4.70×10^{-4} for the 0.25-ML covering.

The adsorption of oxygen on the hollow sites of the lowest formation-energy surface of both alloys is energetically favorable. The computed WF and QE shows that the adsorption of O on the surface has a rather small effect. Nevertheless, the QE could be preserved through careful preparation of surfaces, for example laser cleaning to remove surface-adsorbed oxygen atoms. Here the adsorption of oxygen and formation of the oxide thin film is modeled using a full monolayer of oxygen. This is likely to be significantly more oxygen than is adsorbed in the UHV conditions etc in which the cathode is operated. This suggests that the rather small changes in WF and QE for oxide formation computed here represent an upper bound on the effects of mild oxidation of the CuBa abd CuBa13 surfaces [49].

IV. CONCLUSIONS

Lowering the WF and increasing the QE of photocathode materials is crucial to the future development of FEL facilities. The present work makes use of well-established density-functional theory to combine high WF, stable copper with low WF, unstable barium in two alloys, $Cu_{13}Ba$ and CuBa. The WF of the surfaces cut by the (110) and (111) Miller planes of $Cu_{13}Ba$ are calculated to be slightly lower than that of the bulk alloy. The WF of the most stable (100) surface termination, with an exposed layer of Ba atoms is, however, calculated to be remarkably low; even lower than that of pure Ba, at 1.95 eV.

A Bader charge analysis confirmed that there is significant charge transfer in the alloy from Ba to Cu, and a tendency for Ba to surface segregate produces a large surface dipole. If the dipole vector is pointing out of the surface the WF is lowered, facilitating photoemission, as with the Ba-terminated (100) surface. If the dipole vector is pointing into the surface, as with the Cu-terminated surfaces, the WF is high and photoemission is hindered. These results are confirmed by the QE simulations. The QE of the low WF Ba-terminated (100) surface (5.09×10^{-3}) is over 30 times higher than the high WF Cu-terminated (100) surface (1.52×10^{-4}). The CuBa alloy yielded similar results, the Ba-terminated surfaces showed a low WF and high QE, whereas the Cu-terminated surfaces performed poorly. The best-performing surface, terminating in two layers of Ba atoms, exhibited a very high QE of 1.38×10^{-2} and a WF of 2.20 eV. Compared to pure Mg, which has a QE of about 5.00×10^{-4}, the alloys presented here could offer distinct benefits over other pure metals [50].

It is clear that alloying Cu with Ba results in a significant increase in QE vs pure Cu. The best-performing $Cu_{13}Ba$ surface had a QE over 850 times higher than the best-performing Cu surface, and the best CuBa surface had a QE over 2300 times higher. This is due to the decreased WF and increased DOS in the relevant regions of these surfaces. If these alloys are realized in chemically stable target materials it may allow lower powered drive lasers to be used, thus reducing the complexity and increasing the reliability of the injector system.

Preliminary studies of the formation of oxide layers on the Ba-terminated surfaces suggest that the relatively low levels of oxidation expected in the ultra-high vacuum conditions in which photocathodes are operated is likely to have a rather small effect on the predicted QE of these surfaces.

ACKNOWLEDGMENTS

The authors would like to thank the Imperial College London HPC facility for their help and use of facilities. V.C. is supported by the EPSRC Centre for Doctoral Training in Advance Characterization of Materials (Grant No. EP/L015277/1) and by STFC ASTeC. We acknowledge helpful discussions with M. Surman and E.A. Seddon.

[1] Z. Huang, in *Proceedings, 4th International Particle Accelerator Conference (IPAC 2013): Shanghai, China, May 12–17, 2013* (JACoW, 2013), p. MOYCB101.

[2] J. MacArthur, J. Duris, Z. Huang, and A. Marinelli, in *8th Int. Particle Accelerator Conf. (IPAC'17), Copenhagen, Denmark, 14–19 May, 2017* (JACOW, Geneva, Switzerland, 2017), p. 2848.

[3] D. H. Dowell, I. Bazarov, B. Dunham, K. Harkay, C. Hernandez-Garcia, R. Legg, H. Padmore, T. Rao, J. Smedley, and W. Wan, Cathode R&D for future light sources, Nucl. Instrum. Methods Phys. Res. Sect. A: Accelerators Spectrometers Detectors Assoc. Equip. **622**, 685 (2010).

[4] G. Wang, P. Yang, N. A. Moody, and E. R. Batista, Overcoming the quantum efficiency-lifetime tradeoff of photocathodes by coating with atomically thin two-dimensional nanomaterials, npj 2D Mater. Appl. **2**, 17 (2018).

[5] V. Chang, T. C. Q. Noakes, and N. M. Harrison, Work function and quantum efficiency study of metal oxide thin films on Ag (100), Phys. Rev. B **97**, 155436 (2018).

[6] V. G. Tkachenko, A. I. Kondrashev, and I. N. Maksimchuk, Advanced metal alloy systems for massive high-current photocathodes, Appl. Phys. B **98**, 839 (2010).

[7] B. B. Alchagirov, R. K. Arkhestov, and F. F. Dyshekova, Electron work function in alloys with alkali metals, Tech. Phys. **57**, 1541 (2012).

[8] P. B. Braun and J. L. Meijering, The Copper-rich part of the copper-barium system, Recueil des Travaux Chimiques des Pays-Bas **78**, 71 (1959).

[9] S. J. Clark, M. D. Segall, C. J. Pickard, P. J. Hasnip, M. J. Probert, K. Refson, and M. C. Payne, First principles methods using CASTEP, Z. Kristall. **220**, 567 (2005).

[10] J. P. Perdew, A. Ruzsinszky, G. I. Csonka, O. A. Vydrov, G. E. Scuseria, L. A. Constantin, X. Zhou, and K. Burke, Restoring the Density-Gradient Expansion for Exchange in Solids and Surfaces, Phys. Rev. Lett. **100**, 136406 (2008).

[11] H. J. Monkhorst and J. D. Pack, Special points for Brillouin-zone integrations, Phys. Rev. B **13**, 5188 (1976).

[12] B. Camino, T. Noakes, M. Surman, E. Seddon, and N. Harrison, Photoemission simulation for photocathode design: Theory and application to copper and silver surfaces, Comput. Mater. Sci. **122**, 331 (2016).

[13] C. N. Berglund and W. E. Spicer, Photoemission studies of copper and silver: Theory, Phys. Rev. **136**, A1030 (1964).

[14] F. Roth, C. Lupulescu, E. Darlatt, A. Gottwald, and W. Eberhardt, Angle resolved photoemission from Cu single crystals: Known facts and a few surprises about the photoemission process, J. Electron Spectros. Relat. Phenomena **208**, 2 (2016).

[15] F. Roth, T. Arion, H. Kaser, A. Gottwald, and W. Eberhardt, Angle resolved photoemission from Ag and Au single crystals: Final state lifetimes in the attosecond range, J. Electron Spectros. Relat. Phenomena **224**, 84 (2018).

[16] I. Nagy and P. M. Echenique, Mean free path of a suddenly created fast electron moving in a degenerate electron gas, Phys. Rev. B **85**, 115131 (2012).

[17] J. A. Clarke, D. Angal-Kalinin, N. Bliss, R. Buckley, S. Buckley, R. Cash, P. Corlett, L. Cowie, G. Cox, G. P. Diakun, Others, CLARA conceptual design report, J. Instrum. **9**(05), T05001 (2014).

[18] W. P. Davey, Precision measurements of the lattice constants of twelve common metals, Phys. Rev. **25**, 753 (1925).

[19] A. J. King and G. L. Clark, The crystal structure of barium, J. Am. Chem. Soc. **51**, 1709 (1929).

[20] T. Rodach, K.-P. Bohnen, and K. Ho, First principles calculations of lattice relaxation at low index surfaces of Cu, Surf. Sci. **286**, 66 (1993).

[21] M. P. Punkkinen, Q.-M. Hu, S. K. Kwon, B. Johansson, J. Kollár, and L. Vitos, Surface properties of 3d transition metals, Philos. Mag. **91**, 3627 (2011).

[22] T. Ning, Q. Yu, and Y. Ye, Multilayer relaxation at the surface of fcc metals: Cu, Ag, Au, Ni, Pd, Pt, Al, Surface Sci. **206**, L857 (1988).

[23] H. Davis and J. Noonan, Cu (100) multilayer relaxation, J. Vac. Sci. Technol. **20**, 842 (1982).

[24] D. Adams, H. Nielsen, J. Andersen, I. Stensgaard, R. Feidenhans'l, and J.E. Sorensen, Oscillatory Relaxation of the Cu(110) Surface, Phys. Rev. Lett **49**, 669 (1982).

[25] S. Å. Lindgren, L. Walldén, J. Rundgren, and P. Westrin, Phys. Rev. B **29**, 576 (1984).

[26] J. Luo and B. Legrand, Multilayer relaxation at surfaces of body-centered-cubic transition metals, Phys. Rev. B **38**, 1728 (1988).

[27] J. Yu, X. Lin, J. Wang, J. Chen, and W. Huang, First-principles study of the relaxation and energy of bcc-Fe, fcc-Fe and AISI-304 stainless steel surfaces, Appl. Surface Sci. **255**, 9032 (2009).

[28] D. Jackson, Surface relaxations in cubic metals, Can. J. Phys. **49**, 2093 (1971).

[29] A. Patra, J. E. Bates, J. Sun, and J. P. Perdew, Properties of real metallic surfaces: Effects of density functional semilocality and van der Waals nonlocality, Proc. Natl. Acad. Sci. **114**, E9188 (2017).

[30] J. Wang and S.-Q. Wang, Surface energy and work function of fcc and bcc crystals: Density functional study, Surf. Sci. **630**, 216 (2014).

[31] L. Vitos, A. Ruban, H. L. Skriver, and J. Kollar, The surface energy of metals, Surf. Sci. **411**, 186 (1998).

[32] F. R. De Boer, W. C. M. Mattens, R. Boom, A. R. Miedema, and A. K. Niessen, *Cohesion in Metals* (Elsevier, Amsterdam, 1988).

[33] W. R. Tyson and W. A. Miller, Surface free energies of solid metals: Estimation from liquid surface tension measurements, Surf. Sci. **62**, 267 (1977).

[34] T. Roman and A. Gross, Periodic Density-Functional Calculations on Work-Function Change Induced by Adsorption of Halogens on Cu (111), Phys. Rev. Lett. **110**, 156804 (2013).

[35] H. B. Michaelson, The work function of the elements and its periodicity, J. Appl. Phys. **48**, 4729 (1977).

[36] T. A. Delchar, Oxygen chemisorption on copper single crystals, Surf. Sci. **27**, 11 (1971).

[37] A. Jesche, S. L. Bud'ko, and P. C. Canfield, Single crystal growth and characterization of the large-unit-cell compound $Cu_{13}Ba$, J. Alloys Compd. **587**, 705 (2014).

[38] M. Wendorff and C. Röhr, Polar binary Zn/Cd-rich intermetallics: Synthesis, crystal and electronic structure of A (Zn/Cd) 13 (A = alkali/alkaline earth) and $Cs_{1.34}Zn_{16}$, J. Alloys Compd. **421**, 24 (2006).

[39] D. J. Chakrabarti and D. E. Laughlin, The Ba-Cu (barium-copper) system, Bull. Alloy Phase Diagrams **5**, 564 (1984).

[40] M. L. Fornasini and F. Merlo, The structure of BaCu and SrCu, Acta Crystallogr., Sect. B **36**, 1288 (1980).

[41] W. Tang, E. Sanville, and G. Henkelman, A grid-based Bader analysis algorithm without lattice bias, J. Phys.: Condens. Matter **21**, 84204 (2009).

[42] P. A. Dowben, A. H. Miller, and R. W. Vook, Surface segregation from gold alloys, Gold Bull. **20**, 54 (1987).

[43] W. E. Ford, D. Gao, N. Knorr, R. Wirtz, F. Scholz, Z. Karipidou, K. Ogasawara, S. Rosselli, V. Rodin, G. Nelles, and Florian von Wrochem, Organic dipole layers for ultralow work function electrodes, ACS Nano **8**, 9173 (2014).

[44] F. S. Benneckendorf, S. Hillebrandt, F. Ullrich, V. Rohnacher, S. Hietzschold, D. Jänsch, J. Freudenberg, S. Beck, E. Mankel, W. Jaegermann, Annemarie Pucci, Uwe H. F. Bun, and Klaus Müllen, Structure-property relationship of phenylene-based self-assembled-monolayers

for record low work function of indium tin oxide, J. Phys. Chem. Lett. **9**, 3731 (2018).

[45] X. Duan, O. Warschkow, A. Soon, B. Delley, and C. Stampfl, Density functional study of oxygen on Cu(100) and Cu(110) surfaces, Phys. Rev. B **81**, 075430 (2010).

[46] S. Prada, U. Martinez, and G. Pacchioni, Work function changes induced by deposition of ultrathin dielectric films on metals: A theoretical analysis, Phys. Rev. B **78**, 235423 (2008).

[47] H. J. Freund and G. Pacchioni, Oxide ultra-thin films on metals: New materials for the design of supported metal catalysts, Chem. Soc. Rev. **37**, 2224 (2008).

[48] T. C. Droubay, L. Kong, S. A. Chambers, and W. P. Hess, Work function reduction by BaO: Growth of crystalline barium oxide on Ag (001) and Ag (111) surfaces, Surf. Sci. **632**, 201 (2015).

[49] K. Baptiste, J. Corlett, S. Kwiatkowski, S. Lidia, J. Qiang, F. Sannibale, K. Sonnad, J. Staples, S. Virostek, and R. Wells, A cw normal-conductive rf gun for free electron laser and energy recovery linac applications, Nucl. Instrum. Methods Phys. Res. Sect. A: Accelerators Spectrometers Detectors Assoc. Equip. **599**, 9 (2009).

[50] D. T. Palmer, A Review of Metallic Photocathode-Research, SLAC Publications and Report No. SLAC-TN-05-080 (2005).

[51] S. Foiles, M. Baskes, and M. S. Daw, Embedded-atom-method functions for the fcc metals Cu, Ag, Au, Ni, Pd, Pt, and their alloys, Phys. Rev. B **33**, 7983 (1986).